Effect of Bi2O3-B2O3 as a Sintering aid in Microstructure and Dielectric Properties of Fe2Mo3O12 Electroceramic.

Eduardo Araújo
Universidade Federal do Ceara
Marcelo Silva
Universidade Federal do Ceara
Mauricio Pereira
Universidade Federal do Ceara
Antonio Sombra
Universidade Federal do Ceara
Igor Vasconcelos
Universidade Federal do Ceara
Pierre Fechine (fechine@ufc.br)
https://orcid.org/0000-0002-7822-2354

Research Article

Keywords: LTCC, Fe2Mo3O12, Microwave, Impedance Spectroscopy

Posted Date: July 21st, 2020

DOI: https://doi.org/10.21203/rs.3.rs-45431/v1

Effect of Bi_2O_3-B_2O_3 as a sintering aid in microstructure and dielectric properties of $Fe_2Mo_3O_{12}$ electroceramic.

E. V. Araújo[a], M. A. S. Silva[b], M. S. Pereira[c], A. S. B. Sombra[b], I. F. Vasconcelos[c], P. B. A. Fechine[a,]*.

a: Grupo de Química de Materiais Avançados (GQMat), Departamento de Química Analítica e Físico-Química, Universidade Federal do Ceará – UFC, Campus do Pici, CP 12100, CEP 60451-970, Fortaleza, CE, Brazil.

b: Laboratório de Telecomunicações e Ciência e Engenharia de Materiais (LOCEM), Departamento de Física, Universidade Federal do Ceará, Brazil.

c: Laboratório de Materiais Avançados, Departamento de Engenharia Metalúrgica e de Materiais, Universidade Federal do Ceará, Brazil.

Authors e-mails:

E. V. Araújo eduardo.qufc@hotmail.com

M. A. S. Silva marceloassilva@yahoo.com.br

M. S. Pereira mauriciosousa@alu.ufc.br

A. S. B. Sombra asbsombra@gmail.com

I. F. Vasconcelos ifvasco@ufc.br

*Corresponding Author:

E-mail address: fechine@ufc.br (P. B. A. Fechine)

Phone: +55(85)33669047

Abstract

Molybdates from $A_2Mo_3O_{12}$ family have been widely investigated due to its low sintering temperature, low thermal expansion coefficient, and low dielectric loss. $Fe_2Mo_3O_{12}$ (FMO) is an oxide from this family and widely used in the catalytic field. The aim of this work is to evaluate the influence of the Bi_2O_3-B_2O_3 as a sintering aid in the microstructure and dielectric properties of FMO. The diffraction results showed that the FMO with the monoclinic structure phase was obtained after the calcination process (650 °C). Mössbauer spectroscopy showed the formation of Fe_2O_3 after the sintering process at 800 °C. The scanning electron-microscopic demonstrates an increase of the grain as a function of sintering aid concentration. The samples were analyzed by using the impedance spectroscopy at radiofrequency with temperature variation. The Nyquist diagram obtained in this temperature range was fitted from an equivalent circuit with three R-CPE associations, corresponding to the morphology of the electroceramics. For dielectric properties in the microwave, all the samples showed values of ε_r lower than 10. Values of $Q \times f$ above 14132.35 GHz were achieved. The thermal stability was evaluated by the temperature coefficient of resonant frequency (τ_f). The lowest τ_f values of -6.55 ppm/°C and -4.35 ppm/°C (near-zero) were measured to FMO and FMO mixed with 7.5 wt% Bi_2O_3-B_2O_3, respectively. Based on these results, FMO can be used to low permittivity ceramic for low temperature co-fired ceramics (*LTCC)* applications, antenna substrate, and millimeter-wave range.

Keywords: LTCC; $Fe_2Mo_3O_{12}$; Microwave; Impedance Spectroscopy.

1. Introduction.

The electroceramics emerged as an excellent option for integration and miniaturization of electronic circuits, making smaller and more efficient systems [1]. Due to the advances in telecommunications, it is required that the materials have appropriated dielectric constant (ε_r), low dielectric loss (*tan* δ), near-zero temperature coefficient of resonant frequency (τ_f), high-quality factor (*Q x f*), temperature stable and versatile [2,3]. Electroceramics are widely used in the manufacturing of microwave electronic devices, dielectric substrates, resonators owing to their easy integration in chips [4]. Most of these ceramics require high sintering temperature, which can be a factor that hinders the integration of them into an electronic circuit [5]. Therefore, low temperature co-fired ceramics (LTCC) were developed by adding low quantities of melting temperature oxides, such as Bi_2O_3 [6,7], B_2O_3 [8], TeO_2 [9–11], V_2O_5 [11], among others [12–14], which allows the sintering process below 950 °C.

Recent studies point MoO_3 based electroceramic as an excellent option for *LTCC* application [15–20], with high *Q x f* and low *tan* δ. Nina Joseph and coworkers obtained $CuMoO_4$ sintered at low temperature and completely compatible with the Al electrode and with *Q x f* of 53000 GHz and ε_r of 7.9 [21]. Li-xia Pang *et al* obtained $(K_{0.5}La_{0.5})MoO_4$ with middle ε_r, *Q x f* of 59000 GHz, and 0.0002 of *tan* δ [22]. However, *LTCC* molybdate based materials have high τ_f values [2,5,21,23] and the addition of other compounds are necessary to shift the τ_f to near-zero values. Nina Joseph and coworkers added Ag_2O in $CuMoO_4$ (τ_f = -36 ppm.°C^{-1}) to achieve composite with near-zero τ_f [24].

Molybdates belonging to $A_2M_3O_{12}$ family, where A is a trivalent cation (Fe^{3+}, Al^{3+}, Y^{3+}, and other rare earths) and M is a hexavalent cation (Mo^{6+} or W^{6+}). They have been widely investigated due to their negative or near-zero thermal expansion coefficient (α): $Y_2Mo_3O_{12}$ [25], $Al_2Mo_3O_{12}$, $Sc_2Mo_3O_{12}$ [26], $Fe_2Mo_3O_{12}$ [27], $In_2W_3O_{12}$, $Al_2W_3O_{12}$, $Sc_2W_3O_{12}$ [28], among others. The iron (III) molybdate ($Fe_2Mo_3O_{12}$) has a monoclinic structure at room temperature and shows a monoclinic-to-orthorhombic transition between 510 and 520 °C [29, 30]. Li, Z.W, and coworkers [29] had investigated the $Fe_2Mo_3O_{12}$ (FMO) and they observed the low α of this phase. This property is desirable in the development of electronic devices, where it is needed a material which its dimensions do not change with the temperature changing [31].

FMO has been using to degradation reactions, for rhodamine-B using photocatalyst process, for example [32]. However, the application of FMO, as a potential *LTCC*, has never been

made so far to our knowledge. In this sense, a Bi_2O_3-B_2O_3 mix is used as a sintering aid, the liquid phase of Bi_2O_3 allows the grain growth during the sintering process [33,34], while B_2O_3 is usually employed as flux former [35]. Therefore, the purpose of this study was to evaluate the effect of Bi_2O_3-B_2O_3 mix in the microstructure, structure phase, and dielectric properties at radiofrequency and microwave range of FMO electroceramics.

2. Methodology.

FMO electroceramic was synthesized by solid-sate route using Fe_2O_3 (99%, Sigma Aldrich) and MoO_3 (99.5%, Sigma Aldrich). These starting materials were ground and mixed in agate mortar following the stoichiometry, as described in equation 1.

$$Fe_2O_{3(s)} + 3\ MoO_{3(s)} \rightarrow Fe_2Mo_3O_{12(s)} \quad (1)$$

The mixture was pressed into pellets and calcinated at 650 °C for 16 h. The Bi_2O_3-B_2O_3 sintering aid was prepared using Bi_2O_3 (99.9%, Sigma Aldrich) and B_2O_3 (98%, Sigma Aldrich) and was added in molar ratio 1:1 and mixed in Fritsch Pulverisette 6 planetary mill for 10 h with 370 rpm as rotation speed. Milling was performed in sealed stainless-steel vials under air with stainless-steel balls. A ball mass ratio of 1:9 (Bi_2O_3-B_2O_3 powder mass : ball mass) was used.

For dielectric characterization, the samples were ground and mixed with polyvinyl alcohol (PVA) 10% v/v solution. Bi_2O_3-B_2O_3 was added as sintering aid and the samples were labeled as FMO-X (X= 2.5, 5.0 and 7.5 wt% Bi_2O_3-B_2O_3). Then, each composition was pressed into cylindrical pellets and sintered at 800 °C for 6 h. The volume of these pellets was determined by Archimedes' method to calculate their density. These pellets were polished on both faces and a silver paste (Joint Metal-PC200) was applied on them to ensure the electrical contact.

X-ray powder diffraction (XRPD) patterns were obtained by using a PANalytical diffractometer (Xpert Pro MPD) operating at 40 kV and 40 mA in the Bragg-Brentano geometry, with a Co tube (Ka_1: 1.7889 Å). The diffraction patterns were collected at room temperature from pulverized FMO calcinated and sintered samples. The diffractograms were obtained from 10° to 60° at a step size of 0.013°, with an analysis time of 70 s at each step, in a graphite monochromator in the plane geometry for diffracted beam.

Mössbauer spectra were obtained using transmission mode at room temperature. The ^{57}Co radioactive source in Rh matrix was used mounted in speed controller scanning from -10 $mm.s^{-1}$ to +10 $mm.s^{-1}$ [36]. Spectra were also obtained for FMO calcinated and sintered samples.

Raman spectra were obtained using LabRAM Jobin-Yvon HORIBA spectometer, equipped with liquid nitrogen cooled CCD. A Laser beam was focused in the sample surface using OLYMPUS microscope lens and numeric opening of 0.75, forming a spot of 4 μm^2 under the sample surface. The slits were adjusted to obtain a resolution of 2 cm^{-1}

The surface's microstructure of the FMO based electroceramics was studied by scanning electron microscopy (SEM). Micrograph images were collected at room temperature using a FEG Quanta 450 with Energy-dispersive X-ray spectroscopy (EDS) in the SEM chamber, with an incident electron beam of 20 kV.

For dielectric measurements at the RF range, the samples were evaluated using a Solartron 1260 computer-controlled impedance analyzer as a function of frequency (1 Hz - 10 MHz) at different temperatures (220 °C – 260 °C). On the other hand, the dielectric measurements for the microwave range were evaluated with an Agilent Model PNA N5230A using the Hakki-Coleman method [37]. The Agilent PNA N5230A was also used to measure the τ_f of the FMO as described by Silva and his coworkers [38].

3. Results and Discussion.

In order to confirm the complete calcination of FMO and achieve the crystalline phase, all the samples were analyzed by XRPD technique and compared to $Fe_2Mo_3O_{12}$ (ICSD: 100606, monoclinic, $P2_1/a_1$) crystalline phase. Fig. 1 (a) shows the diffraction pattern of the $Fe_2Mo_3O_{12}$ based ceramics. The first diffractogram is relative to $Fe_2Mo_3O_{12}$ after calcination process and before sintering process (C-FMO). For this sample, only monoclinic $Fe_2Mo_3O_{12}$ was achieved. For FMO, the results demonstrated that a small fraction (2.2 %) of Fe_2O_3 (ICSD: 154190) spurious phase is formed. This behavior was observed for all sintered samples, besides a mass loss in all pellets. Prisco *et al*. related that $A_2Mo_3O_{12}$ molybdates has a thermic decomposition in temperatures higher than 700 °C, forming initial oxides used in the reaction [39]. Therefore, all sintered samples were also analyzed by XRPD to examine the crystalline structure after the sintering process. Diffractograms of FMO, FMO-2.5, FMO-5.0 and FMO-7.5 presented the formation of Fe_2O_3 (ICSD: 154190, Rhombohedral, R-3c) phase,

confirming the thermal decomposition of $Fe_2Mo_3O_{12}$ after the sintering process as described in equation 2.

$$Fe_2Mo_3O_{12(s)} \rightarrow Fe_2O_{3(s)} + 3\ MoO_{3(s)} \quad (2)$$

According to previous results, the Bi_2O_3-B_2O_3 sintering aid mix formed amorphous compound after milling process and probably formed a glass phase after sintering. Therefore, no peaks relative to these phases were found in diffractograms.

Rietveld refinement parameters are presented in Table 1. Low values of agreement indices for all samples shows that the Rietveld refinements were satisfactory, with weighted profile R-factor (R_{WP}) below 20% or between 20 and 30% for samples with two or more phases and χ^2 near to unity [40]. Another factor is the similarity between lattice parameters of samples and the pattern of database, which indicates that structure did not change with addition of Bi_2O_3 and B_2O_3, since Bi^{3+} can substitute Fe^{3+} in octahedral site [41].

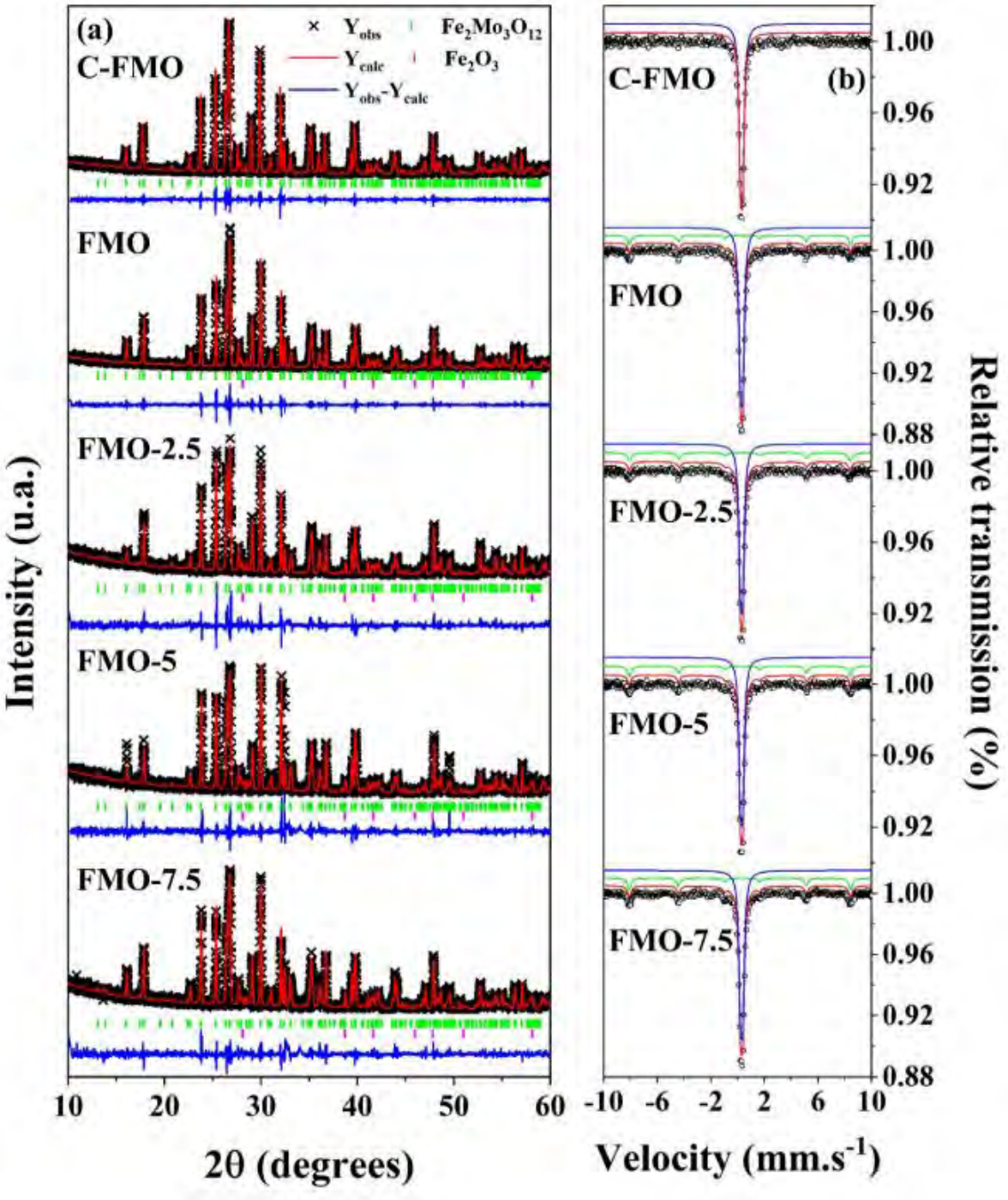

Figure 1: Rietveld refinement of the XRPD (a) with observed (Y_{Obs}) and calculated (Y_{Calc}) intensities and Mössbauer spectra (b) of C-FMO, FMO, FMO-2.5, FMO-5.0 and FMO-7.5.

Sample	Phase	Composition (%)	Lattice parameters							R_{WP} (%)	χ^2
			a (Å)	b (Å)	c (Å)	V (Å^3)	α (°)	β (°)	γ (°)		
C-FMO	$Fe_2Mo_3O_{12}$	100	15.6949(3)	9.2357(1)	18.2226(4)	2157.68(7)	90.0	125.228(1)	90.0	14.68	1.003
FMO	$Fe_2Mo_3O_{12}$	97.8	15.6974(2)	9.2367(1)	18.2230(3)	2158.48(5)	90.0	125.222(1)	90.0	15.08	0.973
	Fe_2O_3	2.2	5.4308(7)	5.4308(7)	5.4308(7)	100.73(2)	55.241(6)	55.241(6)	55.241(6)		
FMO-2.5	$Fe_2Mo_3O_{12}$	88.9	15.6987(4)	9.2376(1)	18.2228(5)	2158.67(9)	90.0	125.229(1)	90.0	20.67	1.366
	Fe_2O_3	11.1	5.4268(1)	5.4268(1)	5.4268(1)	100.70(3)	55.313(9)	55.313(9)	55.313(9)		
FMO-5.0	$Fe_2Mo_3O_{12}$	79.64	15.6992(4)	9.2374(1)	18.2226(5)	2158.96(9)	90.0	125.218(1)	90.0	20.13	1.447
	Fe_2O_3	20.36	5.4292(1)	5.4292(1)	5.4292(1)	100.71(3)	55.266(9)	55.266(9)	55.266(9)		
FMO-7.5	$Fe_2Mo_3O_{12}$	92.9	15.6984(4)	9.2386(1)	18.2272(5)	2159.36(9)	90.0	125.230(2)	90.0	18.89	1.242
	Fe_2O_3	7.1	5.4293(6)	5.4293(6)	5.4293(6)	100.74(2)	55.276(5)	55.276(5)	55.276(5)		

Table 1: Agreement indices and lattice parameter for $Fe_2Mo_3O_{12}$ based ceramics.

The Mössbauer spectra of the samples are shown in Fig. 1 (b). All samples showed a doublet with isomer shift (δ) near to 0.41 mm/s, related to paramagnetic Fe^{3+} ion in high spin state and quadrupole splitting (Δ) at 0.18 mm/s, which is assigned to [FeO_6] sites in $Fe_2Mo_3O_{12}$ monoclinic phase [42]. Spectra of sintered samples showed a low intensity simple sextet, indicating a magnetically ordered state. The high value of hyperfine field (above 51 T), and the values of δ near 0.37 mm/s indicates the presence of α-Fe_2O_3 phase [43–45], which were also found in XRPD analysis. The experimental data of hyperfine parameters are presented in Table 2.

Table 2: Hyperfine parameters for $Fe_2Mo_3O_{12}$ based ceramics.

Sample		δ **(mm/s)**	Δ **(mm/s)**	Γ **(mm/s)**	B_{HF} **(T)**	**Area (%)**
C-FMO	Dublet	0.407	0.177	0.265	-	100
FMO	Dublet	0.408	0.180	0.274	-	86.5
	Sextet	0.369	-0.193	0.288	51.19	13.5
FMO-2.5	Dublet	0.406	0.178	0.266	-	86.0
	Sextet	0.375	-0.240	0.327	51.12	14.0
FMO-5.0	Dublet	0.407	0.180	0.260	-	84.4
	Sextet	0.373	-0.213	0.290	51.30	15.6
FMO-7.5	Dublet	0.408	0.179	0.269	-	81.6
	Sextet	0.366	-0.188	0.308	51.22	18.4

FMO-7.5 showed lower quantity of Fe_2O_3 than FMO-2.5 and FMO-5.0 in XRPD in the analysis, while in Mössbauer spectroscopy it has the higher concentration of such spurious phase. This is probably due the formation of an amorphous glass phase, composed by Fe_2O_3-Bi_2O_3-MoO_3 [46] provided by the thermal decomposition of $Fe_2Mo_3O_{12}$ [39] during sintering process, which cannot be easily observed in diffractograms.

Fig. 2 shows Raman spectra for FMO samples. The $Fe_2Mo_3O_{12}$ monoclinic phase belongs to $P2_1/a_1$ space group with eight molecular formula for unit cell. According to group theory, $Fe_2Mo_3O_{12}$ has 408 modes in Brillouin zone, three of which are acoustic modes and the rest are optical modes which may be described as irreducible representation $\Gamma_{P2_1/a_1} = 102\ A_g + 102\ B_g + 101\ A_u + 100\ B_u$. Only A_g e B_g are Raman

active [30]. For FMO sample, main modes of $Fe_2Mo_3O_{12}$ structure are observed, which reinforces the data obtained from XRPD analysis. Raman spectra of sintered sample FMO is similar to C-FMO. Fe_2O_3, Bi_2O_3 and B_2O_3 phases were not assigned due to its bands being overlapped by $Fe_2Mo_3O_{12}$'s spectrum. Regions between 700 to 900 cm^{-1} and 900 to 1200 cm^{-1} show that some bands keep their shape, intensity and width as it can be seen in Fig. 2. According to Moura *et al*, [30] the band within 200 to 300 cm^{-1} correspond to translational motions of MoO_4 polyhedra, band from 300 to 500 cm^{-1} is related to MoO_4 tetrahedral bendings. Vibrational modes in 783, 803, 822 and 936 cm^{-1} are assigned to asymmetrical stretching of Mo-O bond and modes in 968 e 990 cm^{-1} represents symmetrical stretching of Mo-O bond. All bands and its correlated vibrational modes are presented in Table S1 in Electronic Supplementary Material (ESM).

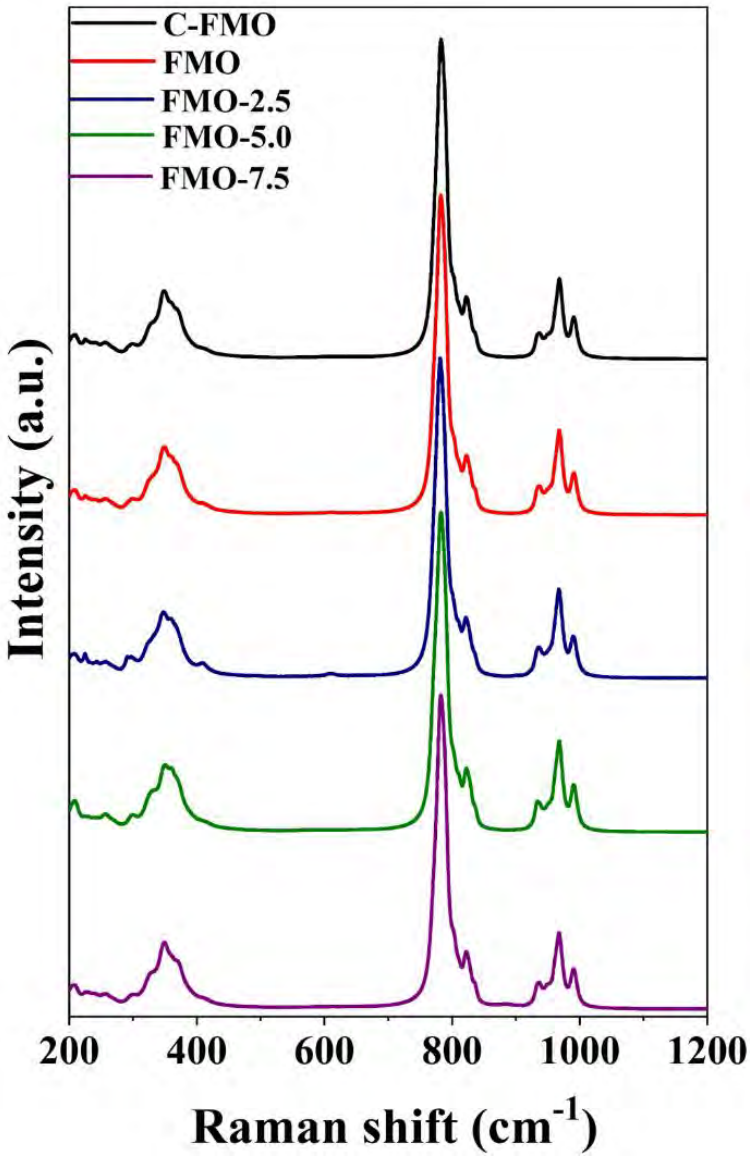

Figure 2: Raman spectra of C-FMO, FMO, FMO-2.5, FMO-5.0 and FMO-7.5.

After sintering process, the pellets were analyzed by SEM at 1000X magnification. Fig. 3 (a) shows the superficial micrograph for FMO. It presents grain size about 3 to 10 μm of diameter, while for FMO-2.5, FMO-5.0 and FMO-7.5 (Fig. 3 (b-d)) are between 20 and 30 μm, as can be seen in the inset of these micrographs. According Tohidifar [33], the sintering aid increases the grain size due the liquid phase flow which promotes the dissolution and diffusion of $Fe_2Mo_3O_{12}$ grains. Although all pellets showed relative density near to 85% ± 2%, which implies that the addition of Bi_2O_3-B_2O_3 as sintering aid does not change the relative density of material in 800 °C sintering process. According to the scanning utilizing EDS technique (Fig. 3 (e) and Fig. S1 in ESM), the surface of all sintered samples are rich in Fe and poor in Mo, which reinforces that thermal decomposition during sintering process volatilizing MoO_3, leaving the Fe_2O_3 on the surface of pellets [39, 47].

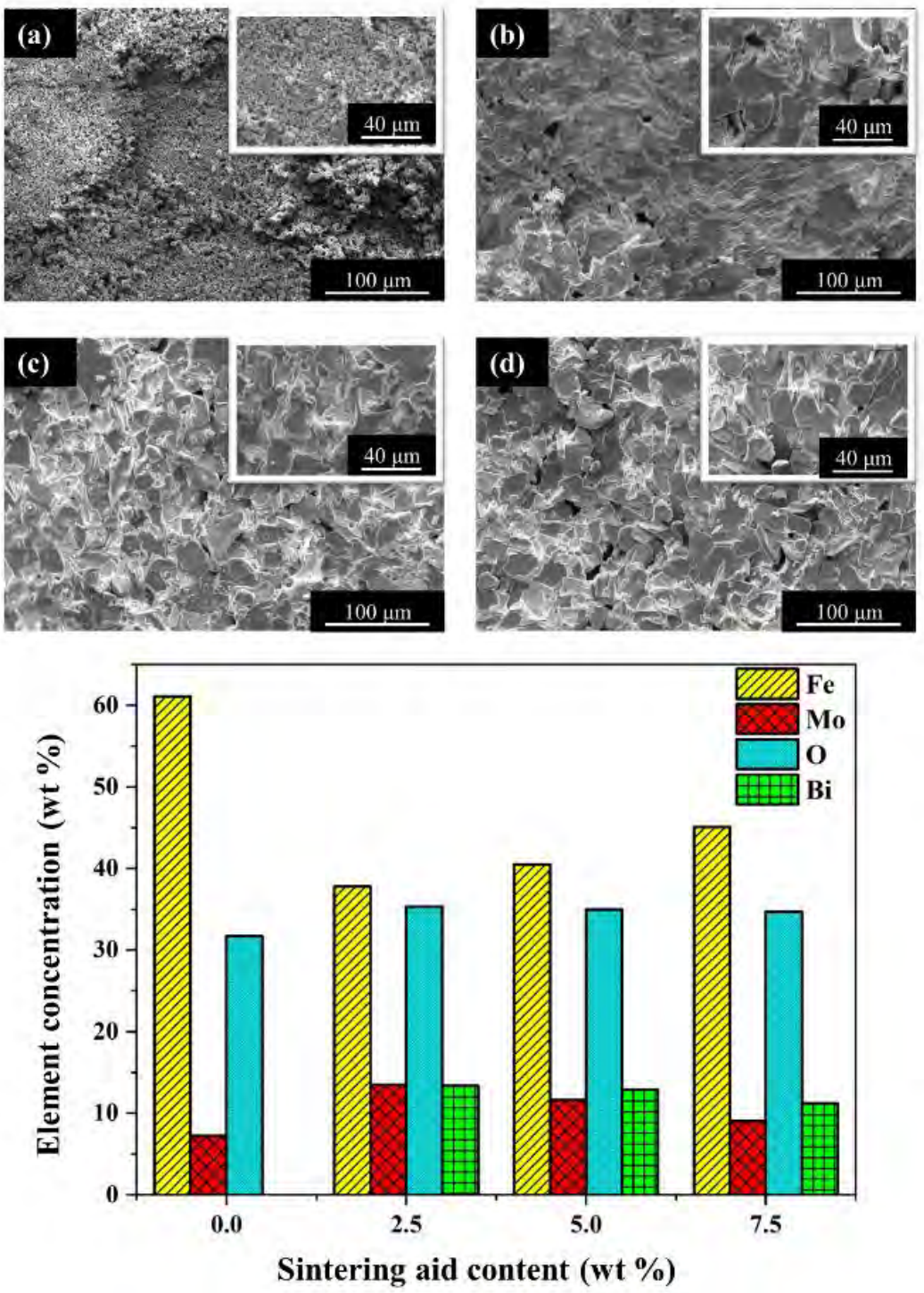

Figure 3: Surface micrograph of (a) FMO, (b) FMO-2.5, (c) FMO-5.0 and (d) FMO-7.5 pellets. Percentage composition in mass ratio *versus* sintering aid content (e).

The broken pellets were also analyzed to investigate inner composition (inside the pellet) and compare to the surface. Fig. S2 of ESM presents micrograph for all the samples and they showed grain size near to 40 μm, higher than those on pellet surface. The scanning using EDS maps are presented in Fig. S3 (ESM) and shows that the concentration of Mo is higher than the ones on surface, which indicates that the pellet's interior does not suffer critical changes in its composition. Table S2 presents the concentration of each element for each sample, for both surface and inside of pellet. Due to the difference on surface and inner composition, EDS analysis of cross section for the FMO sample was made to investigate the inner/surface interface of this material after sintering process and is presented in Fig. 4. Fig. 4 (a) shows the EDS spectrum for pellet surface, while Fig. 4 (b) and Fig. 4 (c) present the EDS spectra for interface and inner, respectively. As can be seen, the amount of Mo is lower on surface than inside the pellet indicating the thermal decomposition of $Fe_2Mo_3O_{12}$ in Fe_2O_3 and MoO_3 and then the MoO_3 volatilization at 700 °C on the surface of the pellet [39,47–49].

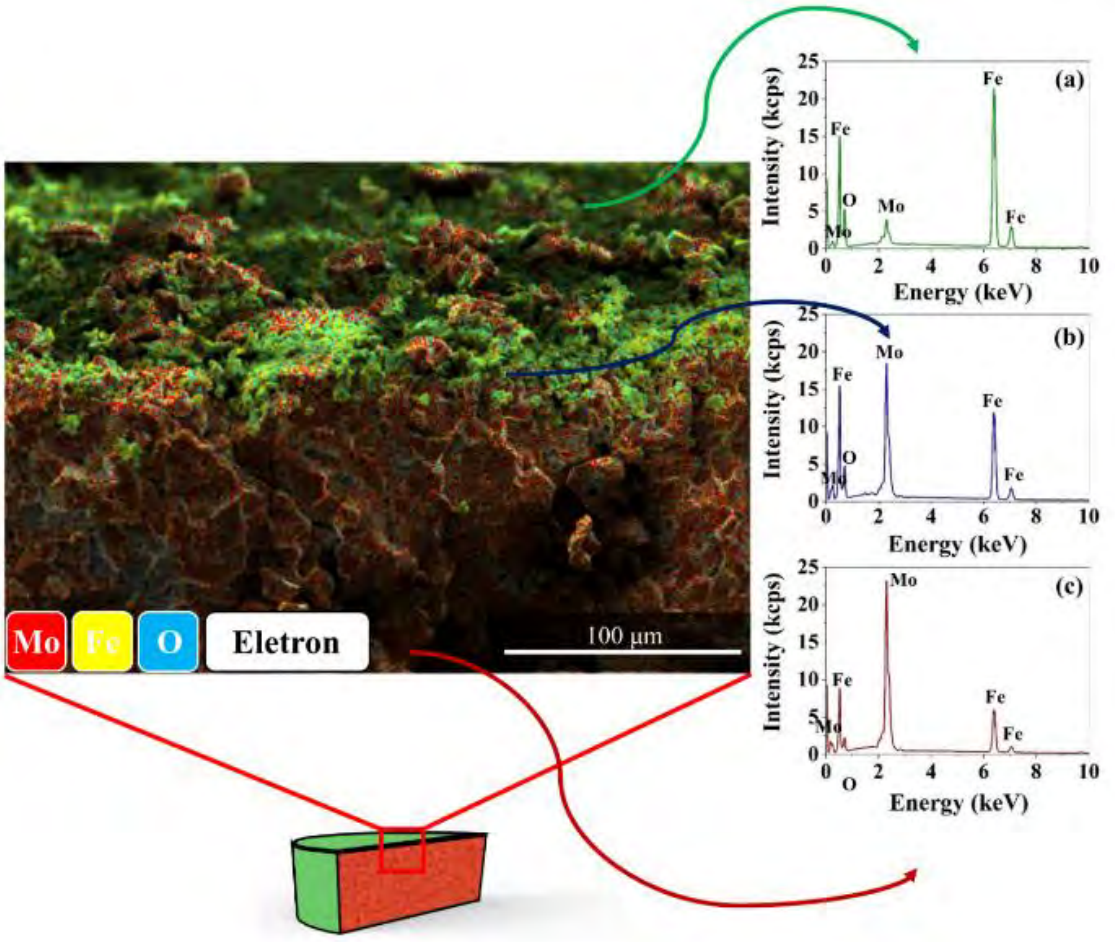

Figure 4: Cylindrical pellet scheme and EDS spectra of different areas. (a) Surface, (b) surface/inner interface and (c) inner.

The results of all structural and morphological characterization allow us to affirm that small part of $Fe_2Mo_3O_{12}$ decomposes thermally in MoO_3 and Fe_2O_3. Superficial MoO_3 volatilize and left surface rich in Fe_2O_3 (observed in mass loss after sintering process and EDS analysis), while inner MoO_3 may form an amorphous glass phase with Fe_2O_3 and Bi_2O_3 [46].

Fig. 5 shows the imaginary part of impedance (*Z''*) spectra and temperature dependency (220 – 260 °C) for the samples. For FMO (Fig. 5 (a)), FMO-2.5 (Fig. 5 (b)) and FMO-5.0 (Fig. 5 (c)) there is a peak about 1 MHz, while for FMO-7.5 (Fig. 5 (d)) this peak appears near to 100 kHz. For the maximum of peak observed in Z" spectrum is observed a shift for higher values with increasing of the temperature what can be related to the relaxation process thermally activated [50]. As can be seen in insets of Fig. 5, the normalized peaks shift to regions of higher frequency.

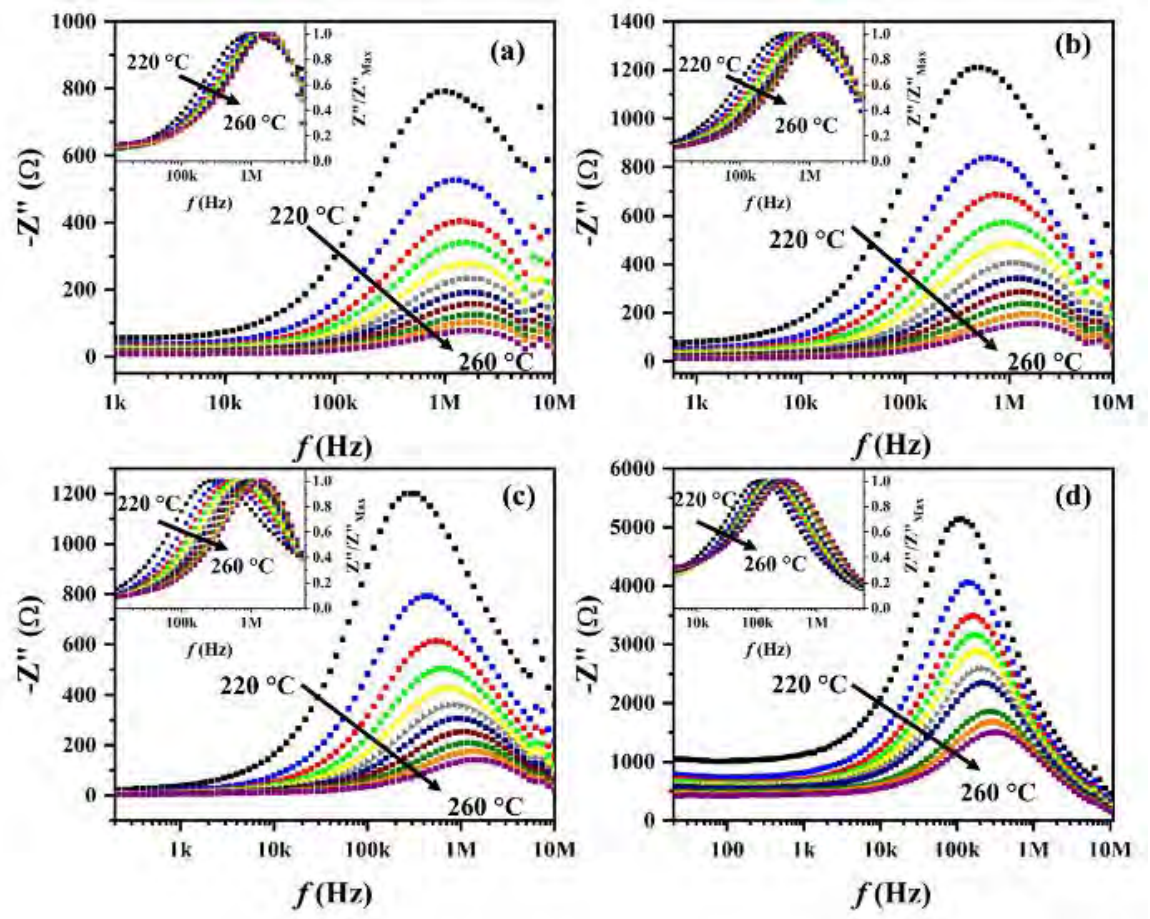

Figure 5: Z" spectra of (a) FMO, (b) FMO-2.5, (c) FMO-5.0 and (d) FMO-7.5. Normalized *Z''* spectrum (inset).

The shift is thermally activated and may be described by Arrhenius' equation:

$$\ln f_{Max} = \ln f_0 - \frac{E_a}{k_b T} \tag{3}$$

where f_{Max} is the frequency when Z'' has a maximum value, f_o is the pre-exponential term, E_a is the activation energy of the process, K_b is the Boltzmann constant and T is temperature [50]. The E_a are determined by the angular coefficient of linear curves in Fig. 6.

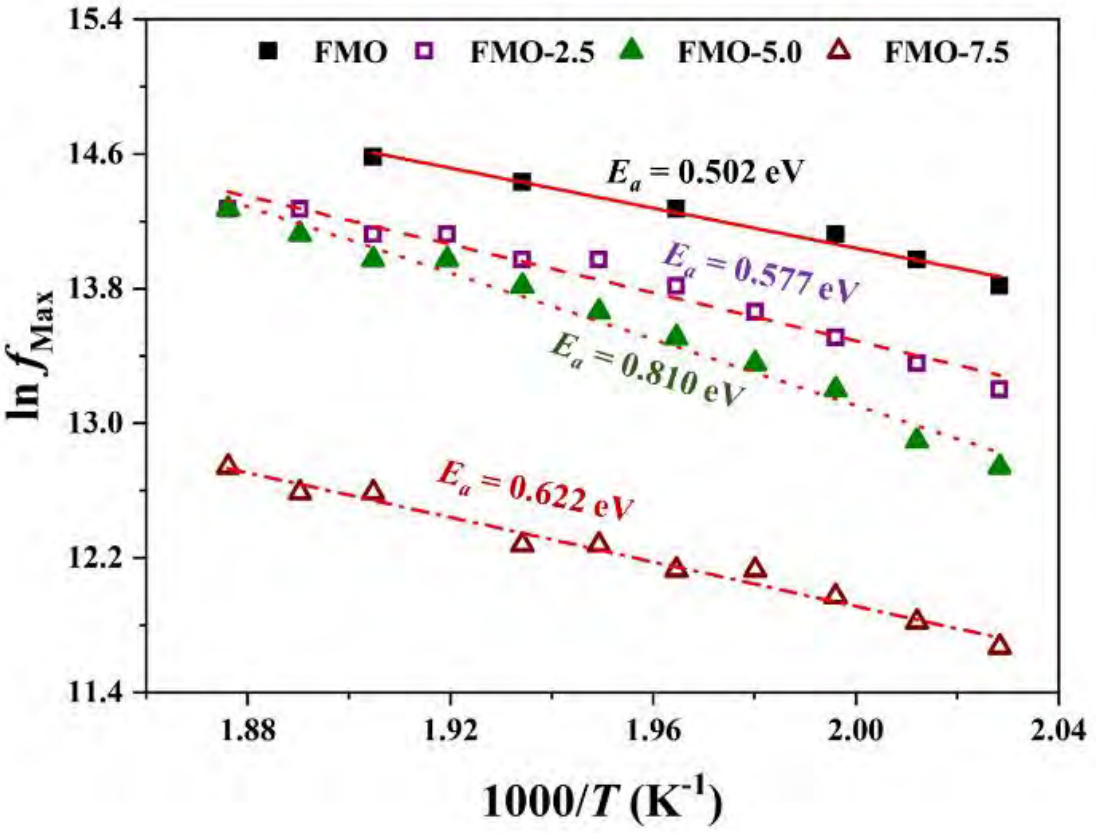

Figure 6: Activation energy of FMO, FMO-2.5, FMO-5.0 and FMO-7.5.

The addition of sintering aid has a direct influence on this process. The E_a increases with rising in sintering aid addition, except for FMO-7.5. This increase is probably due to the higher concentration of Fe_2O_3 spurious phase [51] demonstrated in XRPD and Mössbauer study. FMO presented the lowest energy of 0.502 eV while FMO-5.0 presented energy of 0.810 eV. These E_a values are controlled by Bi_2O_3 and Fe_2O_3 phases formed or added in these composites.

Nyquist's plots (*Z'' versus Z'*) were also analyzed. The spectra presented deformed semicircles in relation to *Z''* axis, corresponding to non-Debye model [52]. The behavior of the ceramic material may be described as resistor-capacitor (R-C), equivalent circuit describing the electric response of grain, grain boundary and electrode effect. As the capacitive contribution does not represent an ideal behavior, the capacitor is substituted by a constant phase element (CPE). The CPE impedance (Z_{CPE}) is described as the following equation [50]:

$$Z_{CPE} = \frac{1}{Q(j\omega)^n} \quad (4)$$

where Q is a proportional factor, ω is the angular frequency and *n* is an empirical exponent with values between 0 (ideal resistor) and 1 (ideal capacitor). All samples were fitted by a non-linear function and are presented in Fig. 7. R_g, R_{gb} and R_e are grain resistance, grain boundary resistance and electrode resistance, respectively, while CPE_g, CPE_{gb} and CPE_e are grain constant phase element, grain boundary constant phase element and electrode constant phase element. Resistive and capacitive contributions of each component (grain, grain boundary and electrode) of the FMO, FMO-2.5, FMO-5.0 and FMO-7.5 are presented in Table S3, S4, S5 and S6 of ESM, respectively.

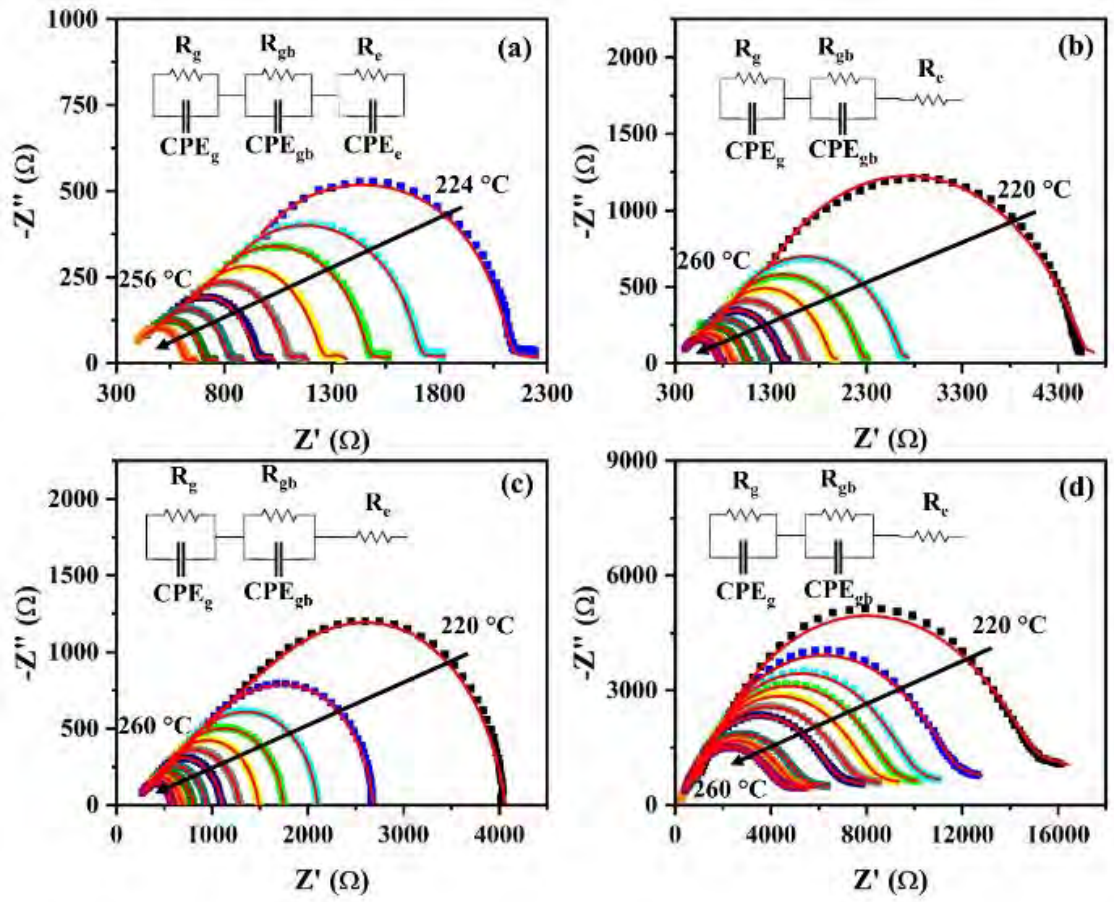

Figure 7: -Z" *versus* Z' of (a) FMO, (b) FMO-2.5, (c) FMO-5.0 and (d) FMO-7.5

As described previously in *Z''* spectra, the resistive contribution of grain, grain boundary and electrode effect decrease with temperature increasing. Grain and electrode are predominantly capacitive due to the fitted parameter *n* (deviation of ideal capacitance) for CPE element with increasing of the temperature [53].

The addition of sintering aid makes the electrode contribution purely resistive, eliminating the capacitive. Moreover, for all samples, the increasing of temperature leads to the decreasing of *n* value for grain boundary contribution, indicating an increasing in resistive contribution of this element. Thermal stability of capacitance (*TCC*) was also determined for all samples using the relation described in Eq. 5 [54].

$$TCC = \frac{C_{100} - C_{25}}{C_{25}.(100-25)}.10^6 \quad (5)$$

Where C_{100} and C_{25} are the capacitance in 100 and 25 °C respectively. Table 3 presents the TCC in 100 Hz, 1 kHz, 10 kHz and 1 MHz frequencies.

Table 3: TCC of FMO, FMO-2.5, FMO-5.0 e FMO-7.5.

Composition	TCC (ppm.°C^{-1})			
	100 Hz	1 kHz	10 kHz	1 MHz
FMO	2986.91	4966.44	-441.12	-1631.75
FMO-2.5	403468.83	210034.36	71681.96	63636.36
FMO-5.0	5637.25	4444.44	-1782.05	-1956.45
FMO-7.5	20747.38	18966.13	-1821.25	-2099.24

FMO-2.5 presents the highest value of TCC for all frequencies. FMO-7.5 is unstable at low frequencies, presenting 20747.38 and 18966.13 ppm.°C^{-1} at 100 Hz and 1 kHz respectively, but is stable at high frequencies. Although FMO, FMO-5.0 and FMO-7.5 presented low value of TCC, at 10 kHz and 1 MHz. According to IEC/EN 60384-8/21 and EIA-RS-198, FMO, FMO-2.5 and FMO-7.5 are potential to be applied as class 1 capacitor at 10 kHz. These ceramics were also analyzed in a microwave frequency range. The temperature coefficient of resonant frequency (τ_f) was determined using the relation described in Eq. 6 [54].

$$\tau_f = \frac{f_{80} - f_{25}}{f_{25}.(80-25)}.10^6 \quad (6)$$

Where f_{80} and f_{25} are the resonant frequency at 80°C and 25 °C, respectively. Table 4 presents the microwave dielectric properties for all samples. Table 4 presents the microwave dielectric properties for all samples. The addition of sintering aid does not imply many changes in microwave dielectric properties of bulks. FMO-2.5 presented the higher ε_r value (9.70) among the samples. Furthermore, FMO based ceramics have ε_r between 9.3 to 9.7, near of Al_2O_3 (ε_r = 9.8), one of the most important oxides used in industry [55]. All compositions showed low values of *tan δ*, and FMO-2.5 presented the smallest value (6.52 x 10^{-4}). This phenomenon can be related to the liquid phase of sintering aid between grain interstice [7]. The greatest dielectric loss of FMO can be

related to the extrinsic loss due to the smaller grains on the surface of the bulk, as can be seen by SEM images [56]. Although all compositions showed a low dielectric loss, which is required for some applications [5]. Moreover, all the composition presented high values of $Q\ x\ f$, and the FMO-2.5 is the one that presented the highest value of 16054.24 GHz, which shows its potential use in microwave devices. τ_f values increase in modulus with increasing sintering aid content, except for FMO-7.5 bulk. FMO and FMO-7.5 showed the lower values of τ_f, probably due to the lower quantity of Fe_2O_3 as a spurious phase which presents a τ_f of -66.64 ppm.° C^{-1} [51]. However, FMO-2.5 and FMO-5.0 presented the highest values of τ_f. This phenomenon is probably related to the high concentration of Fe_2O_3, as it was quantified by XRPD analysis [51, 57].

Table 4: Dielectric properties of FMO, FMO-2.5, FMO-5.0, and FMO-7.5 in the microwave range.

Composition	ε_r	***tan δ***	***Q x f (GHz)***	τ_f **(ppm.°C^{-1})**
FMO	9.33	9.45 x 10^{-4}	14132.35	-6.55
FMO-2.5	9.70	6.52 x 10^{-4}	16054.24	-30.08
FMO-5.0	9.56	6.98 x 10^{-4}	14691.35	-62.99
FMO-7.5	9.49	7.15 x 10^{-4}	14439.76	-4.35

Near-zero τ_f is a very desirable property for resonators and substrates. Recently some researches were taking original strategies to achieve this goal. Castro and coworkers investigated $(Ba_2CoNbO_6)_{1-x}$-$(CaTiO_3)_x$ composite and reached near-zero τ_f at x = 0.37 [58]. Oliveira investigated the effect of $CaTiO_3$ addition in thermal stability of the $BiVO_4$ matrix [59] and Paiva investigated the $Y_3Fe_5O_{12}$-$CaTiO_3$ composite and determined that near-zero τ_f composition [60]. The FMO and FMO-7.5 bulks showed τ_f values of -6.55 and -4.35 ppm.°C^{-1}, respectively. Also, they are characterized as near-zero τ_f, since their values are smaller than ± 10 ppm.°C^{-1}.

4. Conclusion

The solid-state route showed an optimum way to produce the $Fe_2Mo_3O_{12}$ monoclinic phase at 650 °C, which was verified by XRPD, Mössbauer, and Raman spectroscopy. The sintering process at 800 °C was effective in producing dense solids. The SEM images associated with EDS spectra show that the surface of pellets is rich in Fe because of the thermal decomposition of $Fe_2Mo_3O_{12}$ at high temperatures and MoO_3 volatilization. Although the superficial decomposition, the inner structure is preserved, and presence of Bi_2O_3-B_2O_3 allows the growth of superficial grains. Moreover, Bi_2O_3-B_2O_3 sintering aid may prevent higher Mo volatilization, since its content stay close to 7.5%. Nyquist diagrams were observed in a temperature range of 220°C to 260 °C. The grain, grain boundary, and electrode effect contributions were analyzed using an equivalent circuit. Three contributions were obtained from R-CPE to the FMO, while for samples with sintering aid, the capacitive contribution of the electrode vanished away. Furthermore, the Bi_2O_3-B_2O_3 mix increases the resistive contribution of grain in all-ceramic samples compared to FMO. The FMO, FMO-5.0 and FMO-7.5 presented low values of TCC ranging -441.12 to -1824.25 ppm.°C^{-1} and -1631.75 to -2099.24 at 10 kHz and 1 MHz respectively. Microwave characterization presented ε_r within 9.3 and 9.7, and all compositions presented *tan* δ at the magnitude order of 10^{-4} and $Q \times f$ values above 14000 GHz. This implies that they all have the potential to be applied as microwave devices, such as microstrip antenna substrate or dielectric resonator antennas. Moreover, FMO and FMO-7.5 have near-zero τ_f (smaller than ± 10 ppm/°C), making them suitable candidates for dielectric resonator antenna.

Acknowledgements

We gratefully acknowledge the financial support of the following Brazilian agencies for scientific and technological development: CNPq (408790/2016-4), CAPES (Finance Code 001), and Funcap (PNE-0112-00048.01.00/16). In addition, the authors are also grateful for the Central Analítica-UFC/CT-INFRA/MCTI-SISNANO/Pró-Equipamentos, for providing the equipment and technical support for the experiments involving SEM, Laboratório de Difração de raios-X (UFC), and Laboratório de Espectroscopia Vibracional e Microscopia (UFC).

Declaration of competing interest

The authors declare that they have no known competing financial interests or personal relationships that could have appeared to influence the work reported in this paper.

References.

[1] Peng H, Ren H, Dang M, et al. Novel high dielectric constant and low loss PTFE/CNT composites. *Ceram Int* 2018, 14:16556-16560.

[2] Ren J, Bi K, Fu X, Peng Z. Novel Bi_2O_3-added $Al_2Mo_3O_{12}$ composite microwave dielectric ceramics for ULTCC applications. *J Alloys Compd* 2020, 823:153867.

[3] Ren H, Xie T, Wu Z, et al. Crystal structure, phase evolution and dielectric properties in the $Li_2ZnTi_3O_8$-$SrTiO_3$ system as temperature stable high-Q material. *J Alloys Compd* 2019, 797:18–25.

[4] Feng ZB, Tao BJ, Wang WF, et al. Sintering behavior and microwave dielectric properties of $Li_4Mg_3[Ti_{0.8}(Mg_{1/3}Ta_{2/3})_{0.2}]_2O_9$ ceramics with LiF additive for LTCC applications. *J Alloys Compd* 2020, 822:153634.

[5] Sebastian MT, Wang H, Jantunen H. Low temperature co-fired ceramics with ultra-low sintering temperature: a review. *Curr Opin Solid State Mater Sci* 2016, 20:151–170.

[6] Weng Z, AminiRastabi H, Xiong Z, Xue H. Effects of the Bi_2O_3-SiO_2 addition on the sintering behavior and microwave dielectric properties of $Zn_{1.8}SiO_{3.8}$ ceramics. *J Alloys Compd* 2017, 725:1063–1068.

[7] Zhang P, Liao J, Zhao Y, et al. Microstructures and dielectric properties of low permittivity $SrCuSi_4O_{10}$-Bi_2O_3 ceramics for LTCC applications. *J Mater Sci Mater Electron* 2017, 28:4946–4950.

[8] Li T, Segawa H, Ohashi N. Sintering behavior and dielectric properties of $BaTiO_3$ added with BaO-Bi_2O_3-B_2O_3 glass phase. *Ceram Int* 2018, 44:13004–13010.

[9] Cao R, Wu L, Di X, et al. A WLED based on LuAG:Ce^{3+} PiG coated red-emitting K_2SiF_6:Mn^{4+} phosphor by screen-printing. *Opt Mater (Amst)* 2017, 70:92–98.

[10] Chen S, Li W, Zhu D-G. Sintering behaviors, phases, and dielectric properties of MO-TeO_2-V_2O_5 (M= Ca, Sr, Ba) ultralow temperature ceramics. *Mater Res Bull*

2018, 101:29–38.

[11] Masturah M, Norezan I, Yahya AK, et al Effect of V_2O_5–TeO_2 Glass Addition on Dielectric Properties of $CaCu_3Ti_4O_{12}$ Ceramics Prepared by Solid State Method. *Trans Indian Inst Met* 2013, 66:325–328.

[12] Arantes VL. Sintering and microwave properties of zirconium tin titanate doped with select oxides. *J Mater Eng Perform*, 2012 21:1777–1784.

[13] Guan S, Yang H, Zhao Y, Zhang R. Effect of Li_2CO_3 addition in $BiFeO_3$-$BaTiO_3$ ceramics on the sintering temperature, electrical properties and phase transition. *J Alloys Compd* 2018, 735:386–393.

[14] Kim KI, Kim HS, Yun JW. Effects of zinc nitrate as a sintering aid on the electrochemical characteristics of $Sr_{0.92}Y_{0.08}TiO_{3-\delta}$ and $Sr_{0.92}Y_{0.08}Ti_{0.6}Fe_{0.4}O_{3-\delta}$ anodes. *Ceram Int* 2018, 44:4262–4270.

[15] Zhang G, Wang H, Guo J, et al. Ultra-low sintering temperature microwave dielectric ceramics based on Na_2O-MoO_3 binary system. *J Am Ceram Soc* 2015, 98:528–533.

[16] Dhanya J, Suresh EK, Naveenraj R, Ratheesh R. Synthesis and characterization of $Na_5M(MoO_4)_4$ (M= Y, Yb) microwave ceramics for ULTCC applications. *Ceram Int* 2018, 44:6699–6704.

[17] Li H, Huang Z, Cheng L, et al. Structure and dielectric properties of novel low temperature co-fired Bi_2O_3-RE_2O_3-MoO_3 (RE= Pr, Nd, Sm, and Yb) based microwave ceramics. *Ceram Int* 2017, 43:4570–4575.

[18] Zhou D, Randall CA, Wang H, et al. Microwave dielectric ceramics in Li_2O–Bi_2O_3–MoO_3 system with ultra-low sintering temperatures. *J Am Ceram Soc* 2010, 93:1096–1100.

[19] Zuo R, Xu Y, Shi M, et al. A new series of low-temperature cofirable $Li_3Ba_2La_{3(1-x)}Y_{3x}(MoO_4)_8$ microwave dielectric ceramics. *J Eur Ceram Soc* 2018, 38:4677–4681.

[20] Kähäri H, Teirikangas M, Juuti J, Jantunen H. Dielectric properties of lithium molybdate ceramic fabricated at room temperature. *J Am Ceram Soc* 2014, 97:3378–3379.

[21] Joseph N, Varghese J, Siponkoski T, et al. Glass-free $CuMoO_4$ ceramic with excellent dielectric and thermal properties for ultralow temperature cofired ceramic applications. *ACS Sustain Chem Eng* 2016, 4:5632–5639.

[22] Pang L-X, Zhou D, Cai C-L, Liu W-G (2013) Infrared spectroscopy and microwave dielectric properties of ultra-low temperature firing $(K_{0.5}La_{0.5})MoO_4$ ceramics. Mater Lett 92:36–38

[23] Ren J, Bi K, Fu X, Peng Z. Novel $Al_2Mo_3O_{12}$-based temperature-stable microwave dielectric ceramics for LTCC applications. *J Mater Chem C* 2018, 6:11465–11470.

[24] Joseph N, Varghese J, Teirikangas M, et al. Ultra-low sintering temperature ceramic composites of $CuMoO_4$ through Ag_2O addition for microwave applications. *Compos Part B Eng* 2018, 141:214–220.

[25] Romao CP, Miller KJ, Johnson MB, et al. Thermal, vibrational, and thermoelastic properties of $Y_2Mo_3O_{12}$ and their relations to negative thermal expansion. *Phys Rev B* 2014, 90:24305.

[26] Romao CP, Donegan SP, Zwanziger JW, White MA. Relationships between elastic anisotropy and thermal expansion in $A_2Mo_3O_{12}$ materials. *Phys Chem Chem Phys* 2016, 18:30652–30661.

[27] Tamas V, Moats JL, Ushakov SV. Thermochemistry of $A_2M_3O_{12}$ negative thermal expansion materials. *J Mater Res* 2007, 22:2512.

[28] Mary TA, Sleight AW. Bulk thermal expansion for tungstate and molybdates of the type $A_2M_3O_{12}$. *J Mater Res* 1999, 14:912–915.

[29] Li ZY, Song WB, Liang EJ. Structures, Phase Transition, and Crystal Water of $Fe_{2-x}Y_xMo_3O_{12}$. *J Phys Chem C* 2011, 115:17806–17811.

[30] Moura JVB, Pinheiro GS, Freire PTC, et al. High-pressure Raman scattering on $Fe_2(MoO_4)_3$ microcrystals obtained by a hydrothermal method. *Vib Spectrosc* 2016, 87:88–93.

[31] Tummala RR. Ceramic and glass-ceramic packaging in the 1990s. *J Am Ceram Soc* 1991, 74:895–908.

[32] Neelakantan UA, Kalathil SE, Ratheesh R. Structure and microwave dielectric properties of ultralow-temperature cofirable BaV_2O_6 ceramics. *Eur J Inorg Chem* 2015, 2015:305–310.

[33] Tohidifar MR. Improving sintering behavior of MWCNT/$BaTiO_3$ ceramic nanocomposite with Bi_2O_3-B_2O_3 addition. *Ceram Int* 2018, 44:3699–3706.

[34] Le S, Zhang J, Zhu X, et al. Sintering and electrochemical performance of Y_2O_3-doped barium zirconate with Bi_2O_3 as sintering aids. *J Power Sources* 2013, 232:219–223.

[35] Pan Y, Yin J, Zuo K, et al. The sintering behavior and mechanical properties of $CaSiO_3$ bioceramics with B_2O_3 addition. *Ceram Int* 2016, 42:9222–9226.

[36] dos Santos CM, Martins AFN, Costa BC, et al. Synthesis of FeNi Alloy Nanomaterials by Proteic Sol-Gel Method: Crystallographic, Morphological, and Magnetic Properties. *J Nanomater* 2016, 2016.

[37] Hakki BW, Coleman PD. A dielectric resonator method of measuring inductive capacities in the millimeter range. *IRE Trans Microw Theory Tech* 1960, 8:402–410.

[38] Silva MAS, Fernandes TSM, Sombra ASB. An alternative method for the measurement of the microwave temperature coefficient of resonant frequency (τ_f). *J Appl Phys* 2012, 112:74106.

[39] Prisco LP, Pontón PI, Paraguassu W, et al. Near-zero thermal expansion and phase transition in $In_{0.5}(ZrMg)_{0.75}Mo_3O_{12}$. *J Mater Res* 2016, 31:3240.

[40] Deng F, Lin X, He Y, et al. Quantitative phase analysis by the Rietveld method for Forensic science. *J Forensic Sci* 2015, 60:1040–1045.

[41] Cheng YZ, Wu MM, Peng J, et al. Structural studies of Fe doped $Bi_2Mo_3O_{12}$ catalysts using neutron and X-ray powder diffraction. *Mater Technol* 2008, 23:33–38.

[42] Jirak Z, Salmon R, Fournes L, et al. Magnetic and Mössbauer resonance investigations of the weak ferrimagnet iron molybdate ($Fe_2(MoO_4)_3$). *Inorg Chem* 1982, 21:4218–4223.

[43] Yoon S. Preparation and physical characterizations of superparamagnetic maghemite nanoparticles. *J Magn* 2014, 19:323–326.

[44] Sharma VK, Klingelhofer G, Nishida T. Mössbauer spectroscopy: applications in chemistry, biology, and nanotechnology. John Wiley & Sons, 2013.

[45] Bashir AKH, Furqan CM, Bharuth-Ram K, et al. Structural, optical and Mössbauer investigation on the biosynthesized α-Fe_2O_3: study on different precursors. *Phys E Low-dimensional Syst Nanostructures* 2019, 111:152–157.

[46] Iordanova R, Dimitriev Y, Dimitrov V, et al. Glass formation and structure in the system MoO_3–Bi_2O_3–Fe_2O_3. *J Non Cryst Solids* 1998, 231:227–233.

[47] Liu QQ, Yang J, Cheng XN. Study on the preparation of $Fe_2Mo_3O_{12}$ and its negative thermal expansion property. ***Adv Mat Res*** 2011, 287–290: 373–376.

[48] Meyer MK, Thom AJ, Akinc M. Oxide scale formation and isothermal oxidation behavior of Mo–Si–B intermetallics at 600–1000 °C. *Intermetallics* 1999, 7:153–162.

[49] Sun J, Li T, Zhang G-P. Effect of thermodynamically metastable components on mechanical and oxidation properties of the thermal-sprayed $MoSi_2$ based composite coating. *Corros Sci* 2019, 155:146–154.

[50] Trabelsi H, Bejar M, Dhahri E, et al (2017) Effect of oxygen vacancies on $SrTiO_3$ electrical properties. J Alloys Compd 723:894–903.

[51] Silva MAS, Oliveira RGM, Sombra ASB. Dielectric and microwave properties of common sintering aids for the manufacture of thermally stable ceramics. *Ceram Int* 2019, 45:20446–20450.

[52] Macdonald JR, Barsoukov E. Impedance spectroscopy: theory, experiment, and applications. John Wiley, 2017.

[53] Paiva DVM, Silva MAS, Sombra ASB, Fechine PBA. Properties of the Sr_3MoO_6 electroceramic for RF/microwave devices. *J Alloys Compd* 2018, 748:766–773.

[54] Wang D, Zhou D, Song K, et al. Cold-sintered C0G multilayer ceramic capacitors. *Adv Electron Mater* 2019, 5:1900025.

[55] Wang H, Chen J, Yang W, et al. Effects of Al_2O_3 addition on the sintering

behavior and microwave dielectric properties of $CaSiO_3$ ceramics. *J Eur Ceram Soc* 2012, 32:541–545.

[56] Sebastian MT. Dielectric materials for wireless communication. Elsevier, 2010.

[57] Huang C-L, Yang W-R, Chen Y-R. Improvements in the sintering behavior and microwave dielectric properties of $Mg_4Nb_2O_9$ by adding Fe_2O_3. *J Alloys Compd* 2010, 495:L5–L7.

[58] de Castro AJN, Bessa VL, de Morais JE V, et al. A study of the dielectric and electrical properties of the matrix composite [Ba_2CoNbO_6 $(BCNO)_{1-X}$-$CaTiO_3$ $(CTO)_X$]. *Mater Res Bull* 2019, 113:169–174.

[59] Oliveira RGM, Silva RA, de Morais JE V, et al. Effects of $CaTiO_3$ addition on the microwave dielectric properties and antenna properties of $BiVO_4$ ceramics. *Compos Part B Eng* 2019, 175:107122.

[60] Paiva DVM, Silva MAS, de Oliveira RGM, et al. Magneto-dielectric composite based on $Y_3Fe_5O_{12}$–$CaTiO_3$ for radio frequency and microwave applications. *J Alloys Compd* 2019, 783:652–661.

Figures

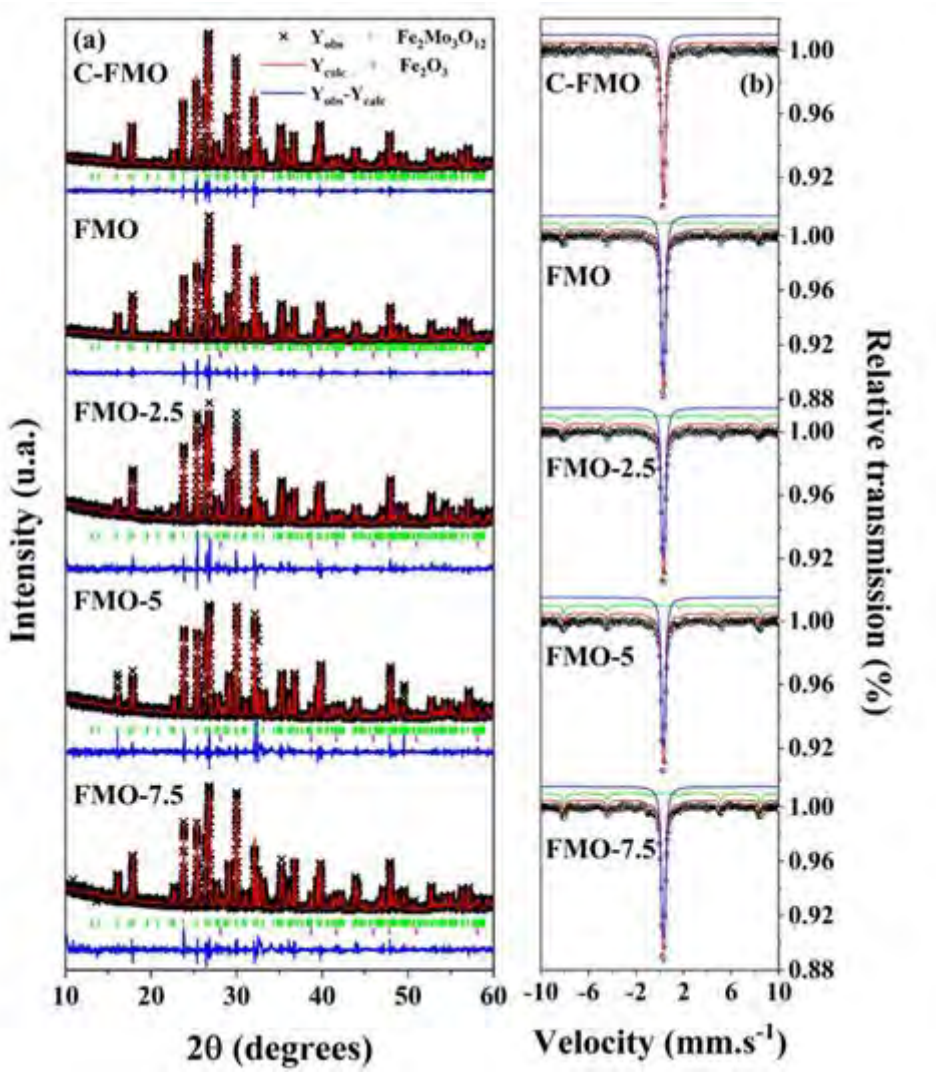

Figure 1

Rietveld refinement of the XRPD (a) with observed (YObs) and calculated (YCalc) intensities and Mössbauer spectra (b) of C-FMO, FMO, FMO-2.5, FMO-5.0 and FMO-7.5.

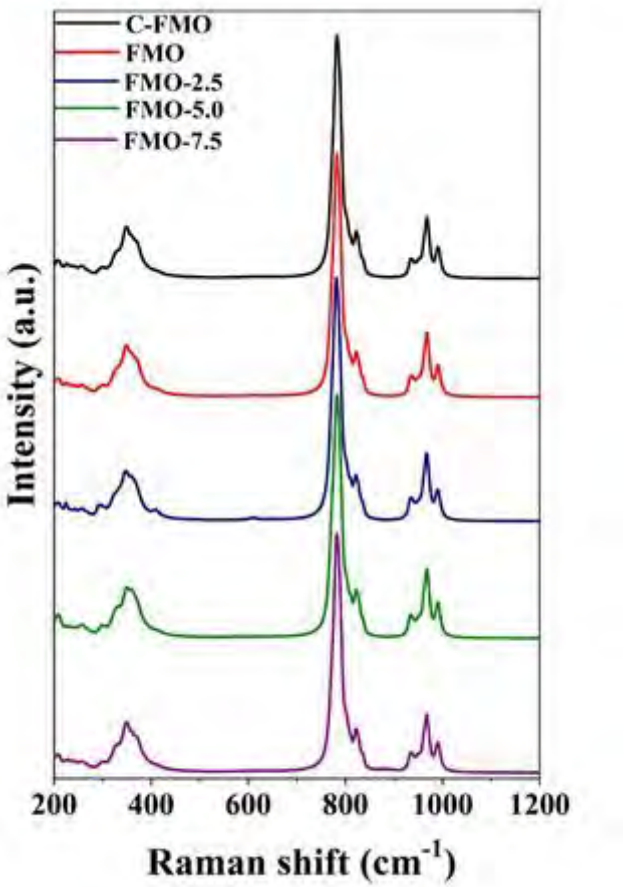

Figure 2

Raman spectra of C-FMO, FMO, FMO-2.5, FMO-5.0 and FMO-7.5.

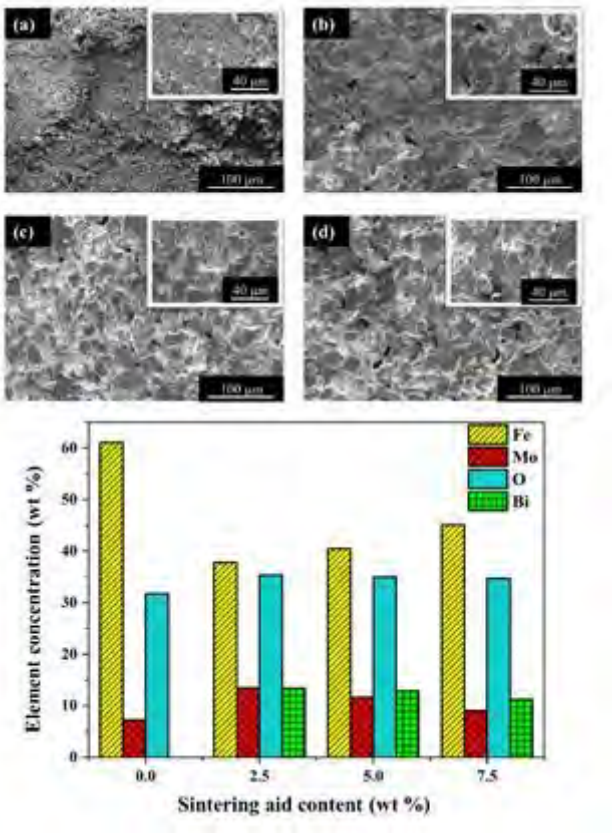

Figure 3

Surface micrograph of (a) FMO, (b) FMO-2.5, (c) FMO-5.0 and (d) FMO-7.5 pellets. Percentage composition in mass ratio versus sintering aid content (e).

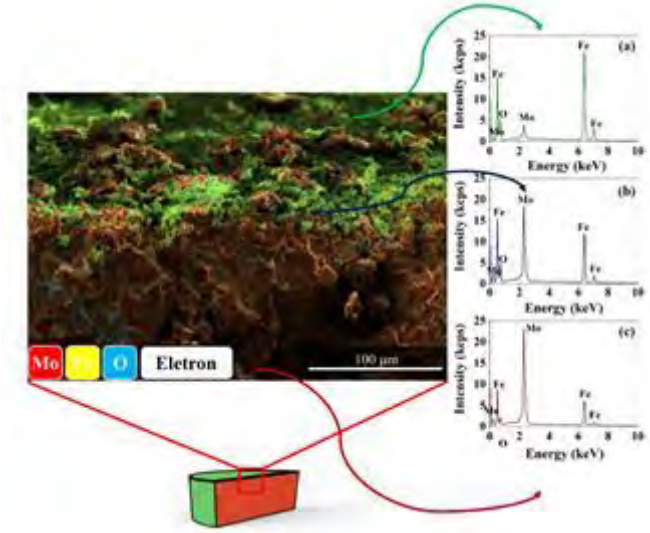

Figure 4

Cylindrical pellet scheme and EDS spectra of different areas. (a) Surface, (b) surface/inner interface and (c) inner.

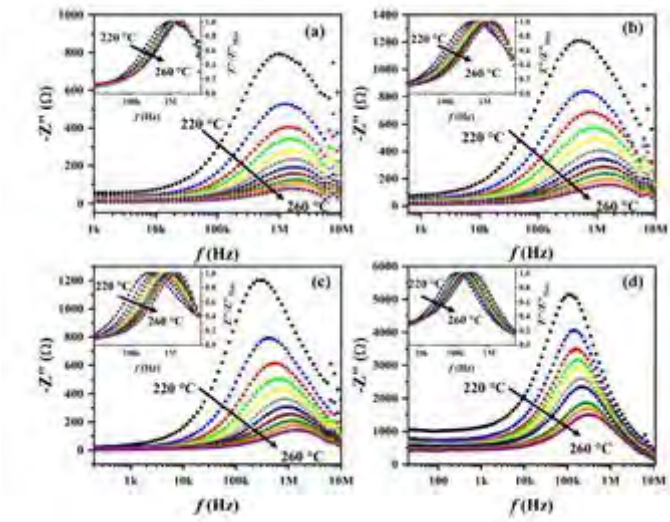

Figure 5

Z” spectra of (a) FMO, (b) FMO-2.5, (c) FMO-5.0 and (d) FMO-7.5. Normalized Z” spectrum (inset).

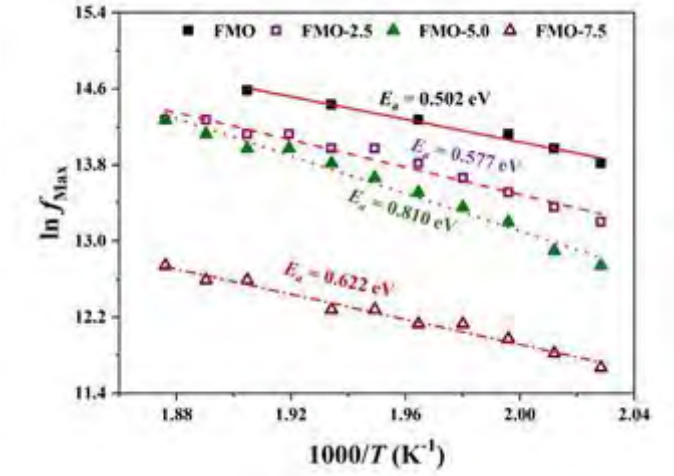

Figure 6

Activation energy of FMO, FMO-2.5, FMO-5.0 and FMO-7.5.

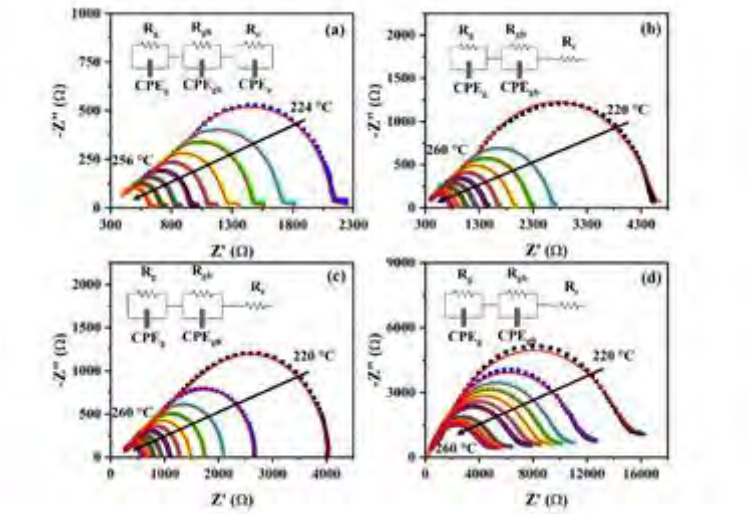

Figure 7

-Z” versus Z’ of (a) FMO, (b) FMO-2.5, (c) FMO-5.0 and (d) FMO-7.5

Supplementary Files

This is a list of supplementary files associated with this preprint. Click to download.

- ElectronicSupplementaryMaterialJACE.docx